HHS Public Access

Author manuscript

Neuroimage. Author manuscript; available in PMC 2020 January 01.

Published in final edited form as:

Neuroimage. 2019 January 01; 184: 45–55. doi:10.1016/j.neuroimage.2018.09.021.

Resting-state white matter-cortical connectivity in non-human primate brain

Tung-Lin Wu[1,2,*], **Feng Wang**[1,3], **Muwei Li**[1], **Kurt G. Schilling**[1,2], **Yurui Gao**[1,3], **Adam W. Anderson**[1,2,3], **Li Min Chen**[1,3], **Zhaohua Ding**[1,3,4], and **John C. Gore**[1,2,3]

[1]Vanderbilt University Institute of Imaging Science, Nashville, TN, United States

[2]Biomedical Engineering, Vanderbilt University, Nashville, TN, United States

[3]Radiology and Radiological Sciences, Vanderbilt University, Nashville, TN, United States

[4]Electrical Engineering and Computer Science, Vanderbilt University, Nashville, TN, United States

Abstract

Numerous studies have used functional magnetic resonance imaging (fMRI) to characterize functional connectivity between cortical regions by analyzing correlations in blood oxygenation level dependent (BOLD) signals in a resting state. However, to date, there have been only a handful of studies reporting resting state BOLD signals in white matter. Nonetheless, a growing number of reports has emerged in recent years suggesting white matter BOLD signals can be reliably detected, though their biophysical origins remain unclear. Moreover, recent studies have identified robust correlations in a resting state between signals from cortex and specific white matter tracts. In order to further validate and interpret these findings, we studied a non-human primate model to investigate resting-state connectivity patterns between parcellated cortical volumes and specific white matter bundles. Our results show that resting-state connectivity patterns between white and gray matter structures are not randomly distributed but share notable similarities with diffusion- and histology-derived anatomic connectivities. This suggests that resting-state BOLD correlations between white matter fiber tracts and the gray matter regions to which they connect are directly related to the anatomic arrangement and density of WM fibers. We also measured how different levels of baseline neural activity, induced by varying levels of anesthesia, modulate these patterns. As anesthesia levels were raised, we observed weakened correlation coefficients between specific white matter tracts and gray matter regions while key features of the connectivity pattern remained similar. Overall, results from this study provide further evidence that neural activity is detectable by BOLD fMRI in both gray and white matter throughout the resting brain. The combined use of gray and white matter functional connectivity could also offer refined full-scale functional parcellation of the entire brain to characterize its functional architecture.

[*]Corresponding author at: Vanderbilt University Institute of Imaging Science, 1161 21st Avenue South, MCN B0104, Nashville, TN, 37232. tung-lin.wu@vanderbilt.edu.

Keywords

fMRI; BOLD; resting-state; white matter; non-human primates

1. INTRODUCTION

Resting-state functional MRI (rsfMRI) based on measuring correlations between blood-oxygenation-level-dependent (BOLD) signals has been widely used to infer functional connectivity between cortical regions (Biswal et al., 1995; Fox and Raichle, 2007). However, the existence of similar resting-state BOLD signals in white matter (WM) has previously been largely overlooked, and little attention has been paid to their potential interpretations. The dearth of WM rsfMRI reports can be partly attributed to the sparse vasculature in WM relative to gray matter (GM), which may be expected to result in reduced hemodynamic effects from the lower blood flow and volume (Jensen et al., 2006). However, the oxygen extraction fraction has been reported to be relatively uniform in the resting brain in both WM and GM (Raichle and Snyder, 2007), and WM is known to contain more glial cells that require energy than GM (Gawryluk et al., 2014; Matute and Ransom, 2012), so there is clearly a possibility of producing BOLD effects in WM. Moreover, vascular challenges such as induced hypercapnia have shown WM responds similarly to GM but with hemodynamic BOLD effects that are smaller than in GM (Macey et al., 2003; Rostrup et al., 2000; Thomas et al., 2014). Furthermore, significant BOLD fMRI hemodynamic response functions were shown and quantified in early visual cortex as well as its apposed WM and pial vasculature (Kim and Ress, 2017). Despite this evidence, several reports have expressed skepticism about the reliability of detecting rsfMRI signals in WM due to the absence of post-synaptic potentials, which have to date been considered the driving sources of BOLD effects. Whatever the precise coupling between BOLD and electrical signals in GM, it is clear that hemodynamic changes in WM are potentially detectable by MRI. As Gawryluk et al. have pointed out, speculations on the origins of BOLD signals in GM do not provide any direct evidence against the possibility of measuring similar phenomena in WM (Gawryluk et al., 2014).

The number of reports claiming successful detection of BOLD signals in WM has risen in recent years. Early reports demonstrated task-induced BOLD signal changes in the corpus callosum (see review Gawryluk et al., 2014) and internal capsule (Gawryluk et al., 2011; Mazerolle et al., 2013b). Notably, a functional topological map of the corpus callosum was generated with fMRI after discrete regions of the corpus callosum were found to be consistently activated (Fabri et al., 2011). Beyond task-derived activations, some recent studies have also investigated resting-state BOLD signals in WM. For example, we previously reported that nearest-neighbor resting state correlations for voxels in WM are anisotropic and we proposed the use of functional correlation tensors to characterize that anisotropy (Ding et al., 2016, 2013). Data-driven methods have also been applied to WM resting-state signals which yielded clusters that closely resemble WM tracts (Mezer et al., 2009). More recently, Peer et al. reported distinct functional networks in WM that were related to both GM functional networks as well as structural WM tracts (Peer et al., 2017). Using independent component analysis, Marussich et al. have also found WM rsfMRI

signals to be hierarchically organized while visual stimuli induced coupling between WM and GM regions in the visual network (Marussich et al., 2017). Similarly, we have shown rsfMRI correlations are significant between specific projection fiber pathways and parcellated cortical regions, and these correlations were further modulated with functional loading (Ding et al., 2018; Wu et al., 2017). Overall, these recent revelations of WM functional activity suggest both stimulus-evoked and resting state BOLD signals can be reliably detected in WM given an appropriate and sensitive technique.

The patterns of activity-related signals in WM appear superficially to follow fiber tracts, but the precise relationships between tractography and functional connectivity based on BOLD signals in WM is unclear. To further interpret and validate WM rsfMRI signals in human brains, appropriate animal models may be useful, and we previously found that rsfMRI WM signal fluctuations were detectable in the brains of anesthetized non-human primates (NHPs) (Wu et al., 2016). We therefore aimed to 1) quantify the resting-state connectivity patterns between cortical volumes and specific WM bundles in NHPs, 2) compare these results directly with diffusion- and histology-derived anatomic connectivities, and 3) examine how different levels of anesthesia modulate these patterns as isoflurane anesthesia level increased and reduced baseline neural activity.

2. MATERIALS AND METHODS

2.1 Animals and preparation.

Eight squirrel monkeys were included in this study. Each animal was initially sedated with ketamine hydrochloride (10 mg/kg)/atropine sulfate (0.05 mg/kg) before being maintained with isoflurane anesthesia (0.5 to 1.5%) delivered in a 70:30 N_2O/O_2 mixture. Animals were intubated and mechanically ventilated (60 bpm). Subsequently, each animal was securely placed on a MR-compatible custom-designed cradle using ear and head bars to prevent motions of the head along with equipment attached for vitals monitoring. Throughout each MRI session, 2.5% dextrose in saline solution (3 ml kg^{-1} hr^{-1}) was infused intravenously and the temperature of each animal was maintained between 37.5 and 38.5°C using a circulating water blanket. Vital signs of the animals were continuously monitored throughout each session – these included ECG heart rate using three leads attached to bilateral arms and one leg, respiratory pattern using a pneumatic pillow, end tidal CO_2, and SpO_2; cardiac and respiratory traces were also recorded and saved in order to correct their effects on BOLD signals (see fMRI pre-processing). At least an hour was allocated for each animal to stabilize physiologically, during which shimming was performed and high resolution anatomical images were acquired. During a typical fMRI data acquisition period, isoflurane was maintained between 0.8 and 0.9%. For fMRI scans examining the effects of anesthesia, isoflurane levels were varied (1.25%, 0.875% and 0.5%). Before acquiring fMRI data at each anesthesia level, at least 10 minutes were also allocated to allow anesthesia stabilization. All procedures were in compliance with the Institutional Animal Care and Use Committee at Vanderbilt University.

2.2 MRI acquisition.

Previously recorded whole brain rsfMRI acquisitions from 8 squirrel monkeys across multiple sessions were analyzed for this study. All scans were performed on a 9.4T magnet using a gradient-echo echo planar imaging (GE-EPI) sequence. A total of 40 runs were acquired across different sessions with slight variations in acquisition parameters:

- TR/TE=500/16ms, 2 shots, 450 volumes, 1×1×1 mm^3, 16 runs
- TR/TE=500/16ms, 2 shots, 300 volumes, 1×1×1 mm^3, 6 runs
- TR/TE=750/16ms, 4 shots, 170 volumes, 1×1×1 mm^3, 8 runs
- TR/TE=1500/16ms, 2 shots, 170 volumes, 1×1×1 mm^3, 10 runs

This set of runs was acquired at anesthesia levels generally between 0.8-0.9% isoflurane and will be labeled as cohort-A. A second set of data (cohort-B) from our previous publication (Wu et al., 2016) was re-analyzed to measure the effects of anesthesia. BOLD images for these studies were acquired with a GE-EPI sequence (TR/TE=750/16ms, 2 shots, 300 imaging volumes, 1×1×1 mm^3) at 1.25%, 0.875% and 0.50% isoflurane levels in three animals with 8, 10 and 9 runs respectively. Anatomical T_2*-weighted images for both sets of data were also collected (TR/TE=500/10ms, NEX=2, 0.125 × 0.125 × 1 mm^3).

2.3 fMRI pre-processing.

Standard fMRI pre-processing of the data similar to that described in our previous publication (Wu et al., 2016) was implemented. Firstly, motion correction (three translations and three rotations) followed by isotropic smoothing with a full width at half maximum of 1.5 mm were performed using *spml2*. Subsequently, 'nuisance' signals derived using principal component analysis of time courses in muscle voxels were extracted to further de-noise the rsfMRI time series. The first three to five signal components that accounted for at least 70% of the cumulative muscle signal variance, along with motion correction parameters, were used as signal regressors in a general linear model to reduce noise contributions to the fMRI signals. RETROICOR corrections (Glover et al., 2000) using both recorded ECG and respiratory traces were subsequently applied to correct for residual cardiac and respiratory interferences. Lastly, signals were bandpass filtered with a pass-band between 0.01-0.08Hz using a Type 2 Chebyshev IIR filter.

2.4 DTI and Histological Connectivity.

DTI and histological connectivity matrices were derived using procedures described in our previous publication (Gao et al., 2017); Figures 2B-C from that are reprinted with permission from Elsevier B.V.. Elements of the DTI connectivity matrix in Figure 2B represent normalized fiber tracts derived using FSL (FMRIB's Diffusion Toolbox, Oxford, UK, http://fsl.fmrib.ox.ac.uk/fsl/fslwiki/FDT/) from all seed points originating in each specific GM volume that are located in the corresponding WM tract; each voxel represents the sum of fiber tracts normalized by the number of seeds and subsequently by the number of occupied voxels. The histological connectivity matrix between WM fiber bundles and cortices was derived from a survey of previous literature that reported anatomical tracer studies in new world monkeys and old world macaques.

2.5 Registration of VALiDATe29 Atlas.

Cortical and WM tract labels from the VALiDATe29 atlas (Schilling et al., 2017) were transformed into fMRI subject space before subsequent correlation analyses. Specifically, high-resolution T_2* weighted anatomical images were first registered to the T_2* weighted template image (VALiDATe29-t2) using an affine linear automatic image registration (AIR) (Woods et al., 1998). With the affine-registered T_2* anatomical image, non-linear registration was performed using large deformation metric mappings (LDMM) (Beg et al., 2005). Using both linear and non-linear transformation matrices, inverses of these transformations were applied to the fMRI labels (VALiDATe29-labels) in reverse order: $LDMM^{-1}$ and then AIR^{-1}. This step produced labels in T_2* anatomical subject space. Lastly, a linear AIR transformation of the T_2* weighted labels into fMRI space was applied. Quality checks were performed by overlaying labels with both anatomical and BOLD images using ITK-SNAP (Yushkevich et al., 2006) for each slice. A minor issue was found where slices towards the top and bottom of the brains were partially sliced due to the re-slicing procedure from *spm12* motion correction. Thus, labels on slices towards the top and bottom edges of the brain were excluded for further analysis. AIR and LDMM transformations were performed using DiffeoMap – MRI Studio developed at Johns Hopkins University (Li, X.; Jiang, H.; and Mori, S.; Johns Hopkins University, www.MriStudio.org or mri.kennedykrieger.org). Left and right peduncle bundles (PB) were not identified given the field-of-view coverage of the rsfMRI acquisitions. It is also important to note two minor differences exist between labels in the atlas (VALiDATe-labels) and in our previous publication on anatomical connectivity (Gao et al., 2017): VALiDATe29 contains both posterior and anterior cingulate cortex as opposed to just the anterior cingulate cortex in Gao et al. Similarly, the secondary somatosensory area, absent in Gao et al., is included with the ventral and rostral parietal cortex (PVR) label. This slight discrepancy exists as these two additional GM labels were not previously identified in Gao et al. but were later captured when creating the atlas across multiple monkeys. Figure 1 shows the data processing pipeline and labels for these registrations.

2.6 Calculation of WM-GM Correlation Matrices.

The atlas identified 57 WM tracts and 18 GM parcellated volumes. For each labeled WM tract–GM volume combination, the Pearson linear correlation coefficients between time courses of each resting state dataset were computed. These were then averaged across runs and animals resulting in a matrix of 75 × 75 values of correlations representing the putative WM-GM connectivity relationships of the squirrel monkey brain. This matrix was further reduced in dimension and rearranged in a configuration analogous to DTI and histological connectivity matrices for comparisons. Variability across runs was quantified by computing standard errors of mean matrices across all animals (shown in Supplementary Figure 1). VALIDATEe29 atlas also includes left and right primary visual cortices (V1) that were absent in our previous publication (Gao et al., 2017). Thus, correlation patterns between left/right V1 and all WM tracts as well as their respective SEM are displayed separately in Supplementary Figure 2.

2.7 Pearson's Correlation and Sørenson-Dice Similarity Coefficient.

In order to quantify overall similarity between the functional and structural connectivity matrices, Pearson's correlation and Sørenson-Dice similarity coefficients (DSCs) were computed. Pearson's correlation was computed between correlation pairs from fMRI and DTI matrices, and were further evaluated for GM-WM with significant correlations ($p<0.05$) as well as with various thresholds applied. For comparisons between rsfMRI and DTI using DSCs, two thresholds (r_{fmri} and d_{dti}) were applied respectively for each modality, generating two binary maps; for any $r > r_{fmri}$ or DTI-fiber-count $> d_{dti}$, a value of '1' is assigned, otherwise '0' is assigned. With the two binary maps, the DSC was computed using the formula:

$$DSC = \frac{2TP}{2TP + FP + FN}$$

where TP, FP and FN denote the true positive, false positive and false negative matrix elements between the two binary matrices respectively. DSC values were subsequently computed with different combinations of r_{fmri} and d_{dti}. Similarly, the histological connectivity map was compared with the rsfMRI connectivity matrix with varying r_{fmri}. DSCs were computed for both cohorts A and B. To determine local maximum values in Table#1, DSCs with $r_{fmri} > 0.05$ and $d_{dti} > 20$ were considered.

2.8 RGB Color Overlay.

While the DSC quantifies overall similarity between two modalities of connectivity, an RGB color overlay method was also used to highlight specific GM-WM pairs that exhibited both high fMRI correlations and DTI fiber densities. Specifically, fMRI (cohort-A) and DTI connectivity matrices were normalized within themselves before each element value of both matrices were represented as different hues of red and blue respectively on the RGB scale; values ranged from [0 0 0] (black) to either [1 0 0] (red) for fMRI or [0 0 1] for DTI (blue). Using properties of additive color mixing, the two matrices were subsequently combined with maximal possible overlay visually represented as magenta [1 0 1]. Thresholds of red and blue values (or normalized connectivity values) were determined separately by calculating the 95^{th} percentile from the normalized fMRI and DTI matrices respectively. Finally, elements of the combined matrix that contain RGB color values greater than both thresholds were identified as GM-WM pairs that exhibit highest degrees of correspondence between fMRI and DTI. In other words, GM-WM pairs that resemble most to the magenta color were identified using red and blue pigment thresholds.

3. RESULTS

3.1 RsfMRI white matter-cortical connectivity.

Averaged temporal correlations between WM bundles and GM are shown in Figure 2A with significance of correlations shown in Figure 2D-E. Each element of the matrix corresponds to a correlation coefficient between a WM-GM pair. It is evident that correlation patterns in the matrix are not randomly distributed, and share notable similarities with diffusion- and histology-derived anatomic connectivities. In addition, representative signals in GM and

WM for a highly and weakly correlated pair are presented in Supplementary Figure 3. Diffusion and histology derived connectivity matrices using almost identical squirrel monkey labels are shown in Figure 2B-C (Gao et al., 2017). By visual inspection it is possible to identify specific GM-WM pairs with large resting-state correlations and high fiber counts in both structural and functional connectivity matrices. For example, strong correlation coefficients between Cingulum (Cing) and anterior cingulate cortex (AC), superior longitudinal fasciculus III (SLFIII) and PVR, as well as between prefrontal cortex (PF) and uncinate fasciculus (UF) showed relatively large fiber density densities. The checkered patterns observed in certain patches of the connectivity matrices are also indicative of bilateral similarity in correlation patterns among the three modalities given how the labels are re-arranged on the axes. Maximum and mean SEM were also computed to be within 0.05 which suggests relatively small variability across runs. The distribution of correlation values between the WM tracts and GM cortical regions are shown in Figure 2F: callosum-body (CCb), optic tract (IIT), Cing, SLFIII, inferior fronto-occipital fasciculus (lFOF), fiber extension of CCb (FCCb), and Coronal Radiata-dorsal posterior (CRdp) had greater correlation values ($r>0.35$) than other WM tracts. RsfMRI GM-WM and their respective SEM matrices for each individual monkey are also displayed along with DSC comparisons between them in Supplementary Figures 4-5.

3.2 Effects of anesthesia on rsfMRI connectivity matrix.

Figure 3 presents resting-state correlation patterns at different isoflurane levels. The averaged correlations between WM and GM regions diminished with increasing anesthesia levels, although patterns of connectivity remain relatively similar between them. Figure 3D-F presents the same correlation matrices with a higher threshold ($r>0.2$) in order to appreciate the connectivity pattern that is retained despite lowered correlation coefficients with elevated anesthesia. Histograms of WM tract correlations with GM (Figure 3G-I) further highlight greater correlation coefficient values at lower anesthesia levels. Lastly, Figure 4 shows statistical comparisons using the non-parametric Wilcoxon Rank-Sum Test between different anesthesia correlation pairs; a p-value less than 0.05 was used to distinguish matrix elements. We found correlation values at 1.25% were statistically less than those at lower isoflurane levels. While the correlation values also dropped between 0.50% and 0.875%, the majority of isoflurane correlation coefficients were found to be largely insignificant (Figure 4).

3.3 Quantitative comparison between rsfMRI with DTI and histological connectivity.

DSCs were computed across different combinations of fMRI and DTI thresholds as shown in the top rows of each subplot in Figure 5 for both cohorts. RsfMRI and histological DSCs were also computed as a function of fMRI thresholds as shown in the bottom of each subplot in Figure 5. DSCs of 0.42 and 0.46 were computed between the rsfMRI correlation matrix (cohort-A) and the DTI and histological connectivities respectively. Statistically significant rsfMRI correlation values were also plotted against normalized fiber counts between GM-WM pairs and displayed as a scatter plot in Figure 6A; correlation between the two modalities were computed to be 0.40 ($p<5 \times 10^{-10}$). In addition, correlations were further computed with varying thresholds of fMRI and DTI (Figure 6B) with an averaged correlation between fMRI and DTI found to be 0.44. While correlation strengths between

WM and GM decreased with increased anesthesia (cohort-B), no trends of DSCs were observed which suggests the pattern of connectivity remains relatively unchanged with anesthesia. Specific peak DSCs values (r_{fmri} >0.05, d_{dti}>20), their corresponding threshold values and significance quantified as probability from random permutations (Supplementary Figure 6) are summarized in Table 1. Supplementary Figure 7 also shows the rsfMRI binary correlation matrix using the optimal fMRI-histology threshold. RGB color overlay comparisons (Figure 7) were also computed to selectively identify GM-WM pairs that demonstrated both high correlations and fiber counts. With pigment thresholds that select for GM-WM pairs that demonstrate high similarity to the maximal overlay color, bilateral PF-UF, AC-Cing, anterior parietal cortex (PA)-SLFIII, and PVR-SLFIII were identified.

4. DISCUSSION

4.1 Similarity between rsfMRI, DTI and histological connectivities.

This study was performed in order to make direct comparisons between apparent WM functional connectivity values derived from rsfMRI and underlying anatomic structures derived from diffusion imaging and histology. We exploited previous results showing how fiber density was related to diffusion tractography and invasive metrics of structure derived from squirrel monkeys that could not be performed in human subjects. We found non-random correlation patterns in a resting state between specific parcellated GM volumes and specific WM tracts in NHP brains, consistent with similar findings in human subjects (Ding et al., 2018). This observation suggests synchronous BOLD signal variations reflecting neural activity between specific cortical volumes and WM bundles in the monkey brain are detectable in a resting state, and that neural activities are encoded in WM BOLD signals similar to cortical fluctuations. In human subjects these patterns changed with functional loading (Ding et al. 2018) whereas in our animal model we were able to show changes with different levels of anesthesia and baseline neural activity. Similarly, Peer et al. found WM and GM networks were highly correlated with correlations reaching above r=0.8 across subjects in a large human group study (Peer et al., 2017). These findings lend further evidence that BOLD signals are present and detectable in WM.

By using an animal model and building on previous studies of the same species, we were also able to compare rsfMRI connectivity patterns with structural connectivity obtained independently from diffusion tractography and histologic data (Figure 2B-C, (Gao et al., 2017)). Quantitative assessments showed modest but positive overall similarity between structural and functional connectivity matrices with statistically significant linear correlation and DSC of 0.40 and 0.42 respectively. While modest overall similarity was found between DTI and functional correlations, specific GM-WM pairs demonstrated high correspondence between structural and functional connectivity matrices, which were identified through RGB overlay (Figure 7). These selected GM-WM pairs are indeed largely consistent with their well-established structural and functional relationships in the literature. For example, we found strong bilateral correlation coefficients and high fiber counts between the Cingulum (Cing) and anterior cingulate cortex (AC). The structural connections between the two regions have previously been confirmed as afferent and efferent fibers of the cingulum have been associated with the cingulate cortex (Baleydier and Mauguiere, 1980; Morris et al.,

1999; Mufson and Pandya, 1984). More specifically, fibers that constitute the subgenual cingulum arise primarily from the AC (Mufson and Pandya, 1984). The functional relevance between them has also been observed: for example, the AC is known to be a critical brain region for pain processing (reviewed by Fuchs et al., 2014) where consistent increased neuronal activity was found in subjects preceding and during an acute noxious stimulus (Hutchison et al., 1999; Iwata, 2005; Koyama et al., 2001). Interestingly, early experimental studies in rats suggested that the impairment of conduction in the Cing bundle disrupted tonic pain (Vaccarino and Melzack, 1989) while cingulotomy in patients have presented considerable success in treating pain in patients (Boccard et al., 2014; Pereira et al., 2014; Santo et al., 1990; Sharma., 1973), which are indicative of their structural and functional relationship, and supports our observation that resting-state correlations parallel high fiber counts and there is a strongly correlated relationship between GM-WM regions and their underlying white matter fiber connections. The same phenomenon is also observed between the uncinate fasciculus (UF) and PFC. The UF, a long-range association fiber that connects the frontal and temporal lobes, has exhibited links to psychopathic traits and behavior (see a review Olson et al., 2015). Alterations of UF have been suggested to impair communication between the frontal and temporal lobe resulting in impaired behaviors such as deficits in decision-making and reversal learning, which are associated functions of the PFC (Olson et al., 2015; Von Der Heide et al., 2013). The other strong bilateral functional-structural correlation pairs identified include PVR-SLFIII and PA-SLFIII. Fibers of the SLFIII have been found to originate in the rostral inferior parietal lobe/supramarginal gyrus, and functional communications between the PVR and other lobes are indeed made possible by the SLFIII (Stuss and Knight, 2002). The connection between the rostral inferior parietal lobe may also be crucial for gestural communication as gestural impairments in ideomotor apraxia are often associated with lesions in either the PVR or underlying white matter (De Renzi, 1989). The functional-structural connection between SLFIII and PA, however, has not been previously well-established. RGB overlay matrices thresholded at lower percentiles (90^{th}, 85^{th}, 80^{th} and 75^{th}) are also displayed in Supplementary Figure 8. Our method of a combined use of GM-WM connectivity may offer a novel way to further refine brain networks and functional architectures. Overall, these findings suggest that resting-state BOLD correlations between specific identified WM fiber tracts and the GM regions to which they connect are directly related to the anatomic arrangement and density of WM fibers.

Despite strong correspondences between structural and functional matrices in specific GM and WM pairs, it is equally important to discuss the presence of inconsistent patterns between them. One possible explanation is the presence of indirect structural connections that are driving strong functional correlations between two regions despite no direct fiber connections. Consistent with this idea, O'Reilly et al. have previously reported in monkeys that whole brain functional connectivity networks were preserved when the anterior commissure was spared after a corpus callosum section. They concluded that functional connectivity in the brain may be driven by cortico-cortical WM connections and that functional patterns can be retained in the presence of indirect structural connections (O'Reilly et al., 2013). More recently, the incorporation of indirect structural pathways have also been shown to be more robust predictors of functional connectivity (Røge et al., 2017).

Another possible reason for the discrepancy shown between functional and structural connectivity is simply that the analysis methods used in this study may not be sensitive enough to tease out all functional-structural relationships between GM and WM (further discussed in Section 4.3).

4.2 Effects of anesthesia on rsfMRI connectivity.

To date, a consensus has yet to be reached on the effects of anesthesia on neural networks, although possible mechanisms have been proposed (Alkire et al., 2008). Specifically, some have found that an increase in anesthesia level reduces the integration of networks as a result of losing synchronization between GM regions and thus lowers correlational patterns (Deshpande et al., 2010; Hutchison et al., 2014; Lu et al., 2007). Indeed, we found in a previous study that the distribution of low frequency fluctuations in WM decreased monotonically with elevated anesthesia levels. Moreover, functional tensor eigenvalues also decreased with increasing level of anesthesia (Wu et al., 2016). In contrast, some studies have found that as anesthesia levels were raised, more synchronous time series and thus elevated correlation values were produced between GM regions (Xiao Liu et al., 2013). Our results support the former interpretation as averaged correlation strengths between WM and GM regions diminished with increasing anesthesia levels. This is evident in Figure 2 where the number of WM tracts with averaged correlations greater than r=0.35 (dashed line) decreased with increasing anesthesia level. Statistical comparisons between 1.25% and the lower isoflurane levels (0.50% and 0.875%) support this finding. While the correlation values dropped with increasing anesthesia level, statistical comparisons between 0.50% and 0.875% isoflurane correlation coefficients were largely insignificant (Figure 4). This observation is consistent with our previous findings (Wu et al., 2016).

The purpose of studying the effects of anesthesia was to further understand how different levels of baseline neural activity altered not just BOLD fluctuations itself (Wu et al., 2016) but also how connectivity patterns between specific GM-WM pairs change. Taking another step in this study, we evaluated how these changes affected their corresponding functional-structural relationship in the whole brain. The extent to which WM and GM are coupled as baseline levels change, and the heterogeneity of responses in GM and WM tracts, are important for interpretations of WM BOLD signals, especially while their existence remains controversial. While the strengths of correlations changed in parallel with varying baseline activity through anesthesia, patterns of connectivity were found to be largely retained. As the amplitudes of BOLD fluctuations are reduced, and if random added noise remains unchanged, we expect absolute values of correlations to decrease, but their relative values should not change. Previous reports have shown that well-defined networks such as the default mode network are observable in different species and whole brain networks are conserved between dissimilar physiological states (Gorges et al., 2017; Liang et al., 2012). We found maximal DSCs comparing rsfMRI correlations to DTI connectivity at the three isoflurane levels to be relatively similar. In fact, an isoflurane level of 1.25% presented the greatest DSC. However, the correlation threshold corresponding to the maximal DSC for 1.25% isoflurane was significantly lower at r = 0.45, an observation that is consistent with the trend that overall correlation strength decreases with increasing anesthesia level. This could of course partly reflect the decreased BOLD signal-to-noise ratio in each time series

as the level of activity decreased rather than inter-regional couplings. Comparisons with histological connectivity, however, showed that anesthesia at 1.25% had the lowest DSC of 0.37 with the lowest significance. In summary, our results suggest that the pattern of connectivity remains relatively unchanged while correlation strengths between WM and GM decreased with increased anesthesia.

4.3 Limitations and future studies.

To date, claims of detecting rsfMRI signals in WM and their interpretation remain somewhat controversial and thus it is important to consider potential confounding factors that may have affected the results of this study. Potential confounds such as cardiac, respiratory, motion or other physiological effects which may have varied with different anesthesia levels were deemed unlikely to have contributed to trends observed in our previous study (Wu et al., 2016). The issue of partial volume averaging is another potential limitation which we have also carefully addressed in previous publications (Ding et al., 2018, 2016; Wu et al., 2016). Similarly in this study, we have performed quality checks after each registration step by 3D-visualization of the quality of the labels overlaid on anatomical images. This was then cross checked by applying the labels of the original BOLD images to further ensure that regions segmented showed minimal partial volume effects. Even if partial volume effects were included, they should account only for 1 to 2 pixels in each tract as outliers in our calculations, given the minimal smoothing kernel of 1.5mm we have used here. Overall, we did not find any major issues in the registration procedure, and this is not surprising given the evaluated accuracy of similar registration pipelines to ours – linear AIR transformation followed by non-linear LDDMM registration to atlases in both humans (Oishi et al., 2009) and animals (Qin et al., 2013). Furthermore, we transformed labels from template space back to subject space for each individual NHP. This prevents large extrapolation of values given the difference in matrix sizes that could result in further mixing of signals between WM and GM. Others have also demonstrated WM activations under minimal partial volume conditions (Fraser et al., 2012; Mazerolle et al., 2013a; Peer et al., 2017). While partial volume effects cannot be completely eliminated and are present in fMRI studies in general, evidence suggests that WM BOLD signals cannot be explained by partial volume effects. The computation of local DSCs required the implementation of thresholds to prevent capturing artificially large Dice coefficients. As shown through randomly mixing functional and structural matrices (Supplementary Figure 8), computing Dice values at either too low or high of a threshold would have had led to results not very different from those obtained from matrices that were randomly permutated. While the trends observed here remain consistent and significant within a reasonable threshold, a different algorithm for comparing functional and structural connectivity methods that does not depend on thresholding may improve and better elucidate their relationship.

Another potential confounding factor in our results is that with higher doses of isoflurane, neurovascular decoupling arises. Specifically, metabolic rate, oxygenation levels and CBF can decrease due to hypotensive effects, which results in lowered BOLD contrast-to-noise ratio and may artificially decrease correlation values. However, we have previously investigated resting-state functional connectivity under such experimental conditions and have found that rsfMRI remains tightly associated with neural activity at these anesthesia

levels (Shi et al., 2017; Wilson et al., 2016). To fully address this issue, we are also currently performing direct neural recordings in WM which would lend further insight to what degree WM BOLD signals reflect neural activity.

Supplementary Material

Refer to Web version on PubMed Central for supplementary material.

ACKNOWLEDGMENTS

Funding: This work was supported by National Institutes of Health grants R01 NS093669 (J.C.G) and NS078680 (J.C.G.)

REFERENCES

Alkire MT, Alkire MT, Hudetz AG, Hudetz AG, Tononi G, Tononi G, 2008 Consciousness and anesthesia. Science 322, 876–80. doi:10.1126/science.1149213 [PubMed: 18988836]

Baleydier C, Mauguiere F, 1980 The duality of the cingulate gyrus in monkey: Neuroanatomical study and functional hypothesis. Brain 103, 525–554. doi:10.1093/brain/103.3.525 [PubMed: 6774795]

Beg MF, Miller MI, Trouvé A, Younes L, 2005 Computing large deformation metric mappings via geodesic flows of diffeomorphisms. Int. J. Comput. Vis 61, 139–157. doi:10.1023/B:VISI.0000043755.93987.aa

Biswal B, Yetkin FZ, Haughton VM, Hyde JS, 1995 Functional Connectivity in the Motor Cortex of Resting. Brain 34, 537–541.

Boccard SGJ, Pereira EAC, Moir L, Van Hartevelt TJ, Kringelbach ML, Fitzgerald JJ, Baker IW, Green AL, Aziz TZ, 2014 Deep brain stimulation of the anterior cingulate cortex: Targeting the affective component of chronic pain. Neuroreport 25, 83–88. doi:10.1097/WNR.0000000000000039 [PubMed: 24100411]

De Renzi E, 1989 Handbook of Neuropsychology. Elsevier Press, Amsterdam, pp. 387–394.

Deshpande G, Kerssens C, Sebel PS, Hu X, 2010 Altered local coherence in the default mode network due to sevoflurane anesthesia. Brain Res. 1318, 110–121. doi: 10.1016/j.brainres.2009.12.075 [PubMed: 20059988]

Ding Z, Huang Y, Bailey SK, Gao Y, Cutting LE, Rogers BP, Newton AT, Gore JC, 2018 Detection of synchronous brain activity in white matter tracts at rest and under functional loading. Proc. Natl. Acad. Sci 115, 595–600. doi:10.1073/pnas.1711567115 [PubMed: 29282320]

Ding Z, Newton AT, Xu R, Anderson AW, Morgan VL, Gore JC, 2013 Spatio-temporal correlation tensors reveal functional structure in human brain. PLoS One 8, e82107. doi:10.1371/journal.pone.0082107 [PubMed: 24339997]

Ding Z, Xu R, Bailey SK, Wu T-L, Morgan VL, Cutting LE, Anderson AW, Gore JC, 2016 Visualizing functional pathways in the human brain using correlation tensors and magnetic resonance imaging. Magn. Reson. Imaging 34, 8–17. doi:10.1016/j.mri.2015.10.003 [PubMed: 26477562]

Fabri M, Polonara G, Mascioli G, Salvolini U, Manzoni T, 2011 Topographical organization of human corpus callosum: An fMRI mapping study. Brain Res. 1370, 99–111. doi:10.1016/j.brainres.2010.11.039 [PubMed: 21081115]

Fox MD, Raichle ME, 2007 Spontaneous fluctuations in brain activity observed with functional magnetic resonance imaging. Nat Rev Neurosci 8, 700–711. doi:nrn2201 [pii]\n10.1038/nrn2201 [PubMed: 17704812]

Fraser LM, Stevens M, Beyea SD, D'Arcy RCN, 2012 White versus gray matter: fMRI hemodynamic responses show similar characteristics, but differ in peak amplitude. BMC Neurosci. 13, 91. doi:10.1186/1471-2202-13-91 [PubMed: 22852798]

Fuchs PN, Peng YB, Boyette-Davis JA, Uhelski ML, 2014 The anterior cingulate cortex and pain processing. Front. Integr. Neurosci 8. doi:10.3389/fnint.2014.00035

Gao Y, Schilling KG, Stepniewska I, Plassard AJ, Choe AS, Li X, Landman BA, Anderson AW, 2017 Tests of cortical parcellation based on white matter connectivity using diffusion tensor imaging. Neuroimage. doi:10.1016/j.neuroimage.2017.02.048

Gawryluk JR, Mazerolle EL, Brewer KD, Beyea SD, D'Arcy RCN, 2011 Investigation of fMRI activation in the internal capsule. BMC Neurosci. 12, 56. doi:10.1186/1471-2202-12-56 [PubMed: 21672250]

Gawryluk JR, Mazerolle EL, D'Arcy RCN, 2014 Does functional MRI detect activation in white matter? A review of emerging evidence, issues, and future directions. Front. Neurosci doi:10.3389/fnins.2014.00239

Glover GH, Li TQ, Ress D, 2000 Image-based method for retrospective correction of physiological motion effects in fMRI: RETROICOR. Magn. Reson. Med 44, 162–167. doi:10.1002/1522-2594(200007)44:1<162::AID-MRM23>3.0.CO;2-E [PubMed: 10893535]

Gorges M, Roselli F, Müller HP, Ludolph AC, Rasche V, Kassubek J, 2017 Functional connectivity mapping in the animal model: Principles and applications of resting-state fMRI. Front. Neurol doi:10.3389/fneur.2017.00200

Hutchison RM, Hutchison M, Manning KY, Menon RS, Everling S, 2014 Isoflurane induces dose-dependent alterations in the cortical connectivity profiles and dynamic properties of the brain's functional architecture. Hum. Brain Mapp 35, 5754–5775. doi:10.1002/hbm.22583 [PubMed: 25044934]

Hutchison WD, Davis KD, Lozano AM, Tasker RR, Dostrovsky JO, 1999 Pain-related neurons in the human cingulate cortex. Nat. Neurosci 2, 403–405. doi:10.1038/8065 [PubMed: 10321241]

Iwata K, 2005 Anterior Cingulate Cortical Neuronal Activity During Perception of Noxious Thermal Stimuli in Monkeys. J. Neurophysiol 94, 1980–1991. doi:10.1152/jn.00190.2005 [PubMed: 15928063]

Jensen JH, Lu H, Inglese M, 2006 Microvessel density estimation in the human brain by means of dynamic contrast-enhanced echo-planar imaging. Magn. Reson. Med 56, 1145–1150. doi:10.1002/mrm.21052 [PubMed: 17029231]

Kim JH, Ress D, 2017 Reliability of the depth-dependent high-resolution BOLD hemodynamic response in human visual cortex and vicinity. Magn. Reson. Imaging 39, 53–63. doi:10.1016/j.mri.2017.01.019 [PubMed: 28137626]

Koyama T, Kato K, Tanaka YZ, Mikami A, 2001 Anterior cingulate activity during pain-avoidance and reward tasks in monkeys. Neurosci. Res 39, 421–430. doi:10.1016/S0168-0102(01)00197-3 [PubMed: 11274741]

Liang Z, King J, Zhang N, 2012 Intrinsic Organization of the Anesthetized Brain. J. Neurosci 32, 10183–10191. doi:10.1523/JNEUROSCI.1020-12.2012 [PubMed: 22836253]

Liu X, Zhu XH, Zhang Y, Chen W, 2013 The change of functional connectivity specificity in rats under various anesthesia levels and its neural origin. Brain Topogr. 26, 363–377. doi:10.1007/s10548-012-0267-5 [PubMed: 23208517]

Lu H, Zuo Y, Gu H, Waltz J. a, Zhan W, Scholl C. a, Rea W, Yang Y, Stein E a, 2007 Synchronized delta oscillations correlate with the resting-state functional MRI signal. Proc. Natl. Acad. Sci. U. S. A 104, 18265–18269. doi:10.1073/pnas.0705791104 [PubMed: 17991778]

Macey PM, Alger JR, Kumar R, Macey KE, Woo MA, Harper RM, 2003 Global BOLD MRI changes to ventilatory challenges in congenital central hypoventilation syndrome. Respir. Physiol. Neurobiol 139, 41–50. doi:10.1016/j.resp.2003.09.006 [PubMed: 14637309]

Marussich L, Lu KH, Wen H, Liu Z, 2017 Mapping white-matter functional organization at rest and during naturalistic visual perception. Neuroimage 146, 1128–1141. doi:10.1016/j.neuroimage.2016.10.005 [PubMed: 27720819]

Matute C, Ransom BR, 2012 Roles of White Matter in Central Nervous System Pathophysiologies. ASN Neuro 4, AN20110060. doi:10.1042/AN20110060

Mazerolle EL, Gawryluk JR, Dillen KNH, Patterson SA, Feindel KW, Beyea SD, Stevens MTR, Newman AJ, Schmidt MH, D'Arcy RCN, 2013a Sensitivity to White Matter fMRI Activation Increases with Field Strength. PLoS One 8. doi:10.1371/journal.pone.0058130

Mazerolle EL, Gawryluk JR, Dillen KNH, Patterson S. a., Feindel KW, Beyea SD, Stevens M, Tynan R, Newman AJ, Schmidt MH, D'Arcy RCN, 2013b Sensitivity to White Matter fMRI Activation Increases with Field Strength. PLoS One 8, 1–12. doi:10.1371/journal.pone.0058130

Mezer A, Yovel Y, Pasternak O, Gorfine T, Assaf Y, 2009 Cluster analysis of resting-state fMRI time series. Neuroimage 45, 1117–1125. doi:10.1016/j.neuroimage.2008.12.015 [PubMed: 19146962]

Morris R, Petrides M, Pandya DN, 1999 Architecture and connections of retrosplenial area 30 in the rhesus monkey (macaca mulatta). Eur. J. Neurosci 11, 2506–2518. doi:10.1046/j.1460-9568.1999.00672.x [PubMed: 10383640]

Mufson EJ, Pandya DN, 1984 Some observations on the course and composition of the cingulum bundle in the rhesus monkey. J. Comp. Neurol 225, 31–43. doi:10.1002/cne.902250105 [PubMed: 6725639]

O'Reilly JX, Croxson PL, Jbabdi S, Sallet J, Noonan MP, Mars RB, Browning PGF, Wilson CRE, Mitchell AS, Miller KL, Rushworth MFS, Baxter MG, 2013 Causal effect of disconnection lesions on interhemispheric functional connectivity in rhesus monkeys. Proc. Natl. Acad. Sci 110, 13982–13987. doi:10.1073/pnas.1305062110 [PubMed: 23924609]

Oishi K, Faria A, Jiang H, Li X, Akhter K, Zhang J, Hsu JT, Miller MI, van Zijl PC, Albert M, Lyketsos CG, Woods R, Toga AW, Pike GB, Rosa-Neto P, Evans A, Mazziotta J, Mori S, 2009 Atlas-based whole brain white matter analysis using large deformation diffeomorphic metric mapping: application to normal elderly and Alzheimer's disease participants. Neuroimage 46, 486–499. doi:S1053-8119(09)00009-3 [pii]\r10.1016/j.neuroimage.2009.01.002 [PubMed: 19385016]

Olson IR, Von Der Heide RJ, Alm KH, Vyas G, 2015 Development of the uncinate fasciculus: Implications for theory and developmental disorders. Dev. Cogn. Neurosci 14, 50–61. doi:10.1016/j.dcn.2015.06.003 [PubMed: 26143154]

Peer M, Nitzan M, Bick AS, Levin N, Arzy S, 2017 Evidence for Functional Networks within the Human Brain's White Matter. J. Neurosci 37, 6394–6407. doi:10.1523/JNEUROSCI.3872-16.2017 [PubMed: 28546311]

Pereira EAC, Paranathala M, Hyam JA, Green AL, Aziz TZ, 2014 Anterior cingulotomy improves malignant mesothelioma pain and dyspnoea. Br. J. Neurosurg 28, 471–474. doi:10.3109/02688697.2013.857006 [PubMed: 24199940]

Qin YY, Li MW, Zhang S, Zhang Y, Zhao LY, Lei H, Oishi K, Zhu WZ, 2013 In vivo quantitative whole-brain diffusion tensor imaging analysis of APP/PS1 transgenic mice using voxel-based and atlas-based methods. Neuroradiology 55, 1027–1038. doi:10.1007/s00234-013-1195-0 [PubMed: 23644540]

Raichle ME, Snyder AZ, 2007 A default mode of brain function: A brief history of an evolving idea. Neuroimage 37, 1083–1090. doi:10.1016/j.neuroimage.2007.02.041 [PubMed: 17719799]

Røge R, Ambrosen KS, Albers KJ, Eriksen CT, Liptrot MG, Schmidt MN, Madsen KH, Mørup M, 2017 Whole brain functional connectivity predicted by indirect structural connections, in: 2017 International Workshop on Pattern Recognition in Neuroimaging, PRNI 2017. doi:10.1109/PRNI.2017.7981496

Rostrup E, Law I, Blinkenberg M, Larsson HBW, Born AP, Holm S, Paulson OB, 2000 Regional differences in the CBF and BOLD responses to hypercapnia: A combined PET and fMRI study. Neuroimage 11, 87–97. doi:10.1006/nimg.1999.0526 [PubMed: 10679182]

Santo JL, Arias LM, Barolat G, Schwartzman RJ, Grossman K, 1990 Bilateral cingulumotomy in the treatment of reflex sympathetic dystrophy. Pain 41, 55–59. doi:10.1016/0304-3959(90)91109-V [PubMed: 1693763]

Schilling KG, Gao Y, Stepniewska I, Wu T-L, Wang F, Landman BA, Gore JC, Chen LM, Anderson AW, 2017 The VALiDATe29 MRI Based Multi-Channel Atlas of the Squirrel Monkey Brain. Neuroinformatics. doi:10.1007/s12021-017-9334-0

Shi Z, Wu R, Yang P-F, Wang F, Wu T-L, Mishra A, Chen LM, Gore JC, 2017 High spatial correspondence at a columnar level between activation and resting state fMRI signals and local field potentials. Proc. Natl. Acad. Sci. U. S. A 114, 5253–5258. doi:10.1073/pnas.1620520114 [PubMed: 28461461]

Stuss DT, Knight RT, 2002 Principles of frontal lobe function. Ann. Phys. (N. Y) 54, 616. doi:10.1093/acprof: oso/9780195134971.001.0001

Sharma T, Absence of cognitive deficits from bilateral cingulotomy for intractable pain in humans. Tex Med. 1973;69:79–82.

Thomas BP, Liu P, Park DC, van Osch MJP, Lu H, 2014 Cerebrovascular reactivity in the brain white matter: magnitude, temporal characteristics, and age effects. J. Cereb. Blood Flow Metab 34, 242–7. doi:10.1038/jcbfm.2013.194 [PubMed: 24192640]

Vaccarino AL, Melzack R, 1989 Analgesia produced by injection of lidocaine into the anterior cingulum bundle of the rat. Pain 39, 213–219. doi:10.1016/0304-3959(89)90008-0 [PubMed: 2594399]

Von Der Heide RJ, Skipper LM, Klobusicky E, Olson IR, 2013 Dissecting the uncinate fasciculus: Disorders, controversies and a hypothesis. Brain. doi:10.1093/brain/awt094

Wilson GH, Yang PF, Gore JC, Chen LM, 2016 Correlated inter-regional variations in low frequency local field potentials and resting state BOLD signals within S1 cortex of monkeys. Hum. Brain Mapp 37, 2755–2766. doi:10.1002/hbm.23207 [PubMed: 27091582]

Woods RP, Grafton ST, Watson JDG, Sicotte NL, Mazziotta JC, 1998 Automated image registration: II. Intersubject validation of linear and nonlinear models. J. Comput. Assist. Tomogr 22, 153–165. doi:10.1097/00004728-199801000-00028 [PubMed: 9448780]

Wu T-L, Wang F, Anderson AW, Chen LM, Ding Z, Gore JC, 2016 Effects of anesthesia on resting state BOLD signals in white matter of non-human primates. Magn. Reson. Imaging 34, 1235–1241. doi:10.1016/j.mri.2016.07.001 [PubMed: 27451405]

Wu X, Yang Z, Bailey SK, Zhou J, Cutting LE, Gore JC, Ding Z, 2017 Functional connectivity and activity of white matter in somatosensory pathways under tactile stimulations. Neuroimage 152, 371–380. doi:10.1016/j.neuroimage.2017.02.074 [PubMed: 28284801]

Yushkevich PA, Piven J, Hazlett HC, Smith RG, Ho S, Gee JC, Gerig G, 2006 User-guided 3D active contour segmentation of anatomical structures: Significantly improved efficiency and reliability. Neuroimage 31, 1116–1128. doi:10.1016/j.neuroimage.2006.01.015 [PubMed: 16545965]

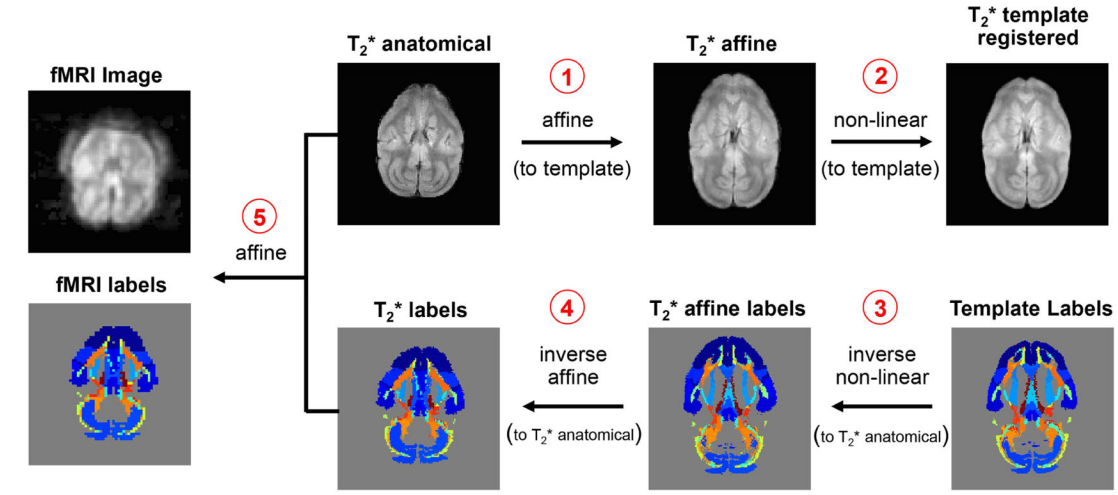

Gray Matter
PF: prefrontal cortex
AC: anterior cingulate cortex
PC: posterior cingulate cortex
SMA: supplemental motor area
PM: premotor cortex
M1: primary motor cortex
PA: anterior parietal cortex
PP: posterior parietal cortex
PVR: ventral and rostral parietal cortex
S2: secondary somatosensory cortex

White Matter
CCg: Corpus callosum-genu
CCb: Corpus callosum-body
CCs: Corpus callosum-splenium
ICa: Internal Capsule – anterior limb
ICg: Internal Capsule – genu
ICp: Internal Capsule – posterior limb
F: Fornix
PC: Posterior Commissure
AC: Anteriror Commissure
EC: External capsule
Cing: Cingulum
UF: Uncinate Fasc.
IIT: Optic tract
SLFI: Superior Longitudinal Fasc. I
SLFII: Superior Longitudinal Fasc. II
SLFIII: Superior Longitudinal Fasc. III
MLF: Middle Longitudinal Fasc.
ILF: Inferior Longitudinal Fasc.
IFOF: Inferior Fronto-Occipital Fasc.
FMn: Forceps Minor
FCCb: Fiber extension of CCb
FMj: Forceps Major
CRa: Coronoal Radiata-anterior
CRs: Coronal Radiata-superior
CRdp: Coronal Radiata-dorsal posterior
PB: Peduncle bundle
CSp: Cortical-spinal cord

Figure 1:

Registration pipeline of VALiDATe29 squirrel monkey atlas labels to fMRI subject space. Labels for WM tracts were transformed into fMRI space by first performing affine linear automatic image registration (AIR) followed by non-linear registration (Large Deformation Metric Mappings (LDMM)) of T_2* anatomical images to the VALiDATe29 squirrel monkey atlas. Inverse of these transformation matrices were subsequently applied – $LDMM^{-1}$ and then AIR^{-1} – to bring the labels back into T_2* anatomical subject space. Finally, labels are transformed to BOLD subject space using affine linear AIR. Abbreviations for parcellated cortical volumes and white matter tracts are shown at the bottom.

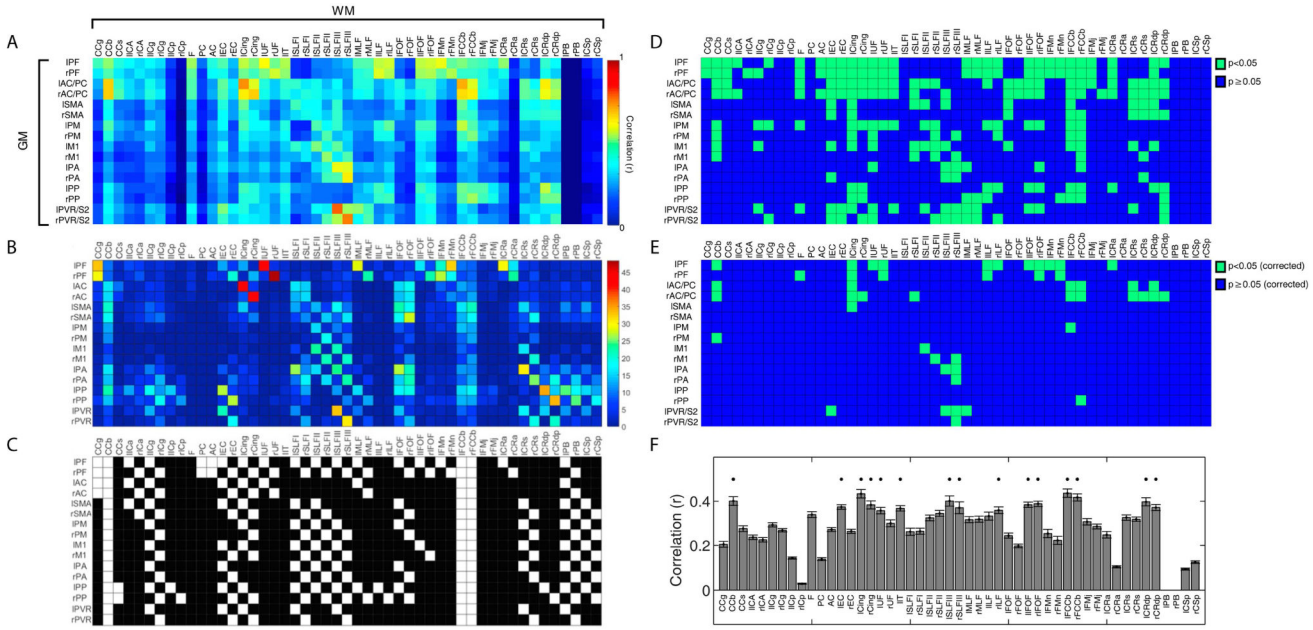

Figure 2:

Connectivity matrices between identified gray matter regions and white matter (WM) tracts. Rows and columns of each matrix represent cortical regions and WM bundles respectively (N=8 monkeys, n=40 runs, cohort-A). (A) Resting-state functional connectivity pattern; each pixel value represents a Pearson's correlation value. (B) Connectivity derived from DTI tractography; each pixel value represents normalized sum of WM fiber density. (C) Histological connectivity represented with a binary map: 0 (black, no observed histological connectivity) and 1 (white, observed histological connectivity). Figures 2B-C are reprinted from with permission from Elsevier; abbreviations for each label can also be found in the reference and Figure 1. (D-E) Significances of rsfMRI correlations in Figure 2A between GM-WM pairs. Green and blue voxels indicate p-values less than 0.05 and p-values greater than or equal to 0.05 respectively without (D) and with (E) False Discovery Rate correction. (F) Averaged temporal correlations of WM tracts across cortical regions for cohort-A. Standard errors of mean are shown as error bars in the bar plot. Asterisks on top of bars indicate WM tracts with mean correlation coefficients greater than 0.35.

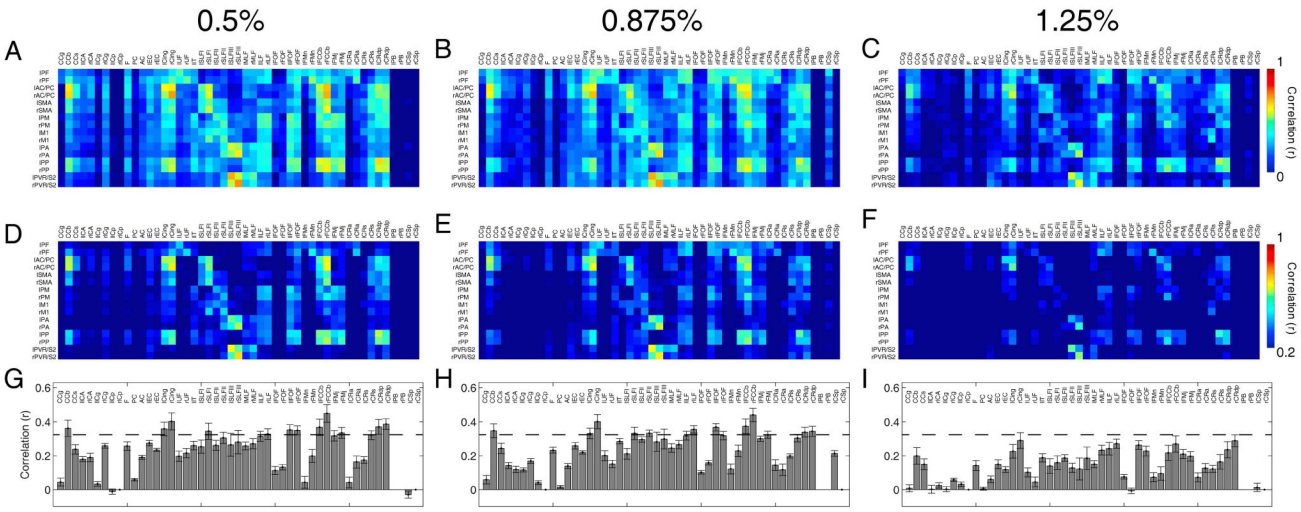

Figure 3:

Connectivity matrices between identified gray matter regions and WM tracts at different anesthesia levels. Pixels from each matrix represent Pearson's correlation values. Resting-state connectivity patterns between specific WM bundles and cortical regions were computed at 0.5%, 0.875% and 1.25% isoflurane levels with n=8, 10, and 9 runs respectively (N=3 monkeys) thresholded at (A-C) r=0 and (D-F) r=0.2. (G-I) Averaged correlations across cortical regions to white matter tracts for each anesthesia level. Error bars on the bar plots represent standard error of mean while dashed line cuts through the bar plots at r=0.35.

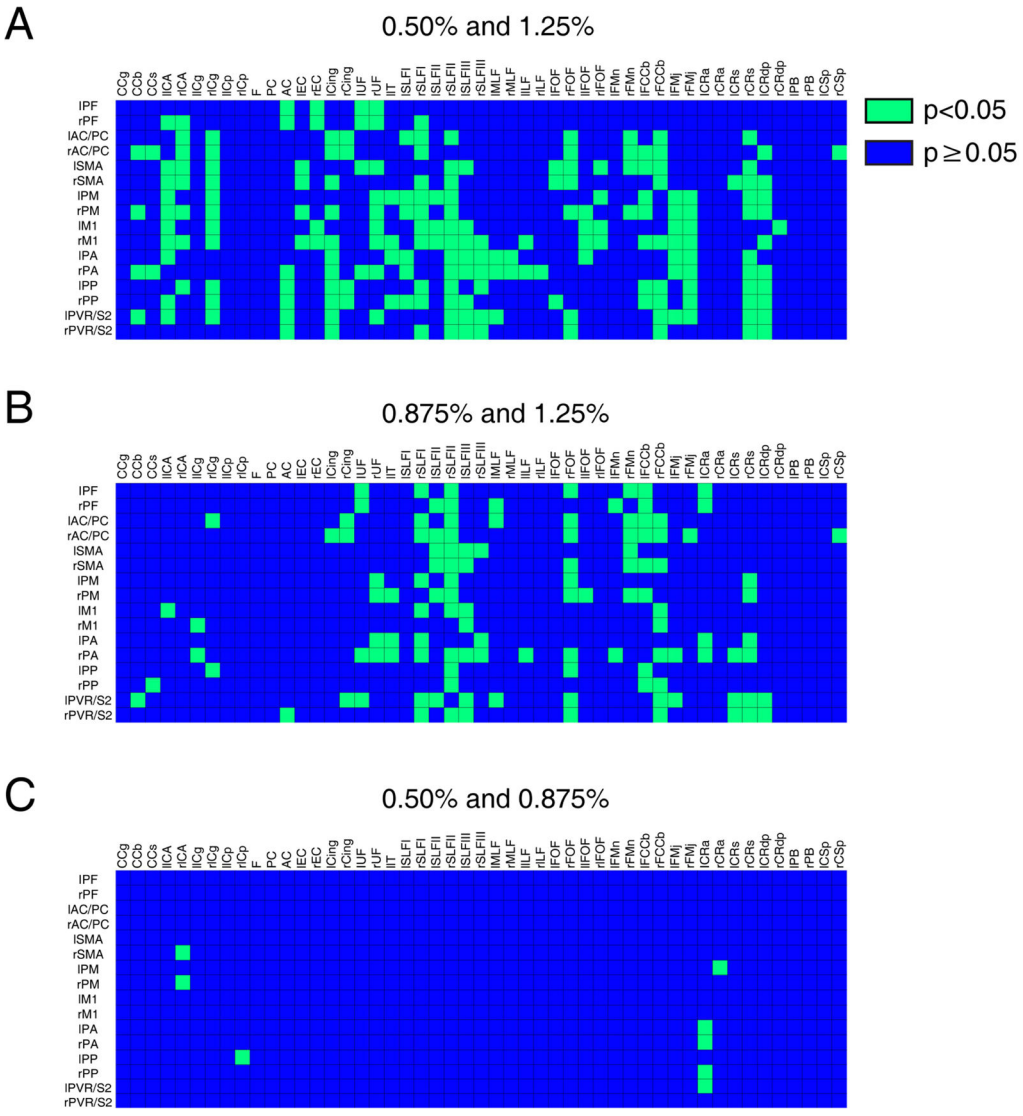

Figure 4:

Non-parametric Wilcoxon Rank-Sum Test between correlation coefficients at different anesthesia levels. Comparison of correlation values between WM tracts and GM with different anesthesia pairs: (A) 0.50% and 1.25%, (B) 0.875% and 1.25%, and (C) 0.50% and 0.875%. Green and blue voxels represent p-values less than 0.05 and p-values greater than or equal to 0.05 respectively. There are a total of 215, 210 and 8 green voxels for (A), (B) and (C) matrices respectively.

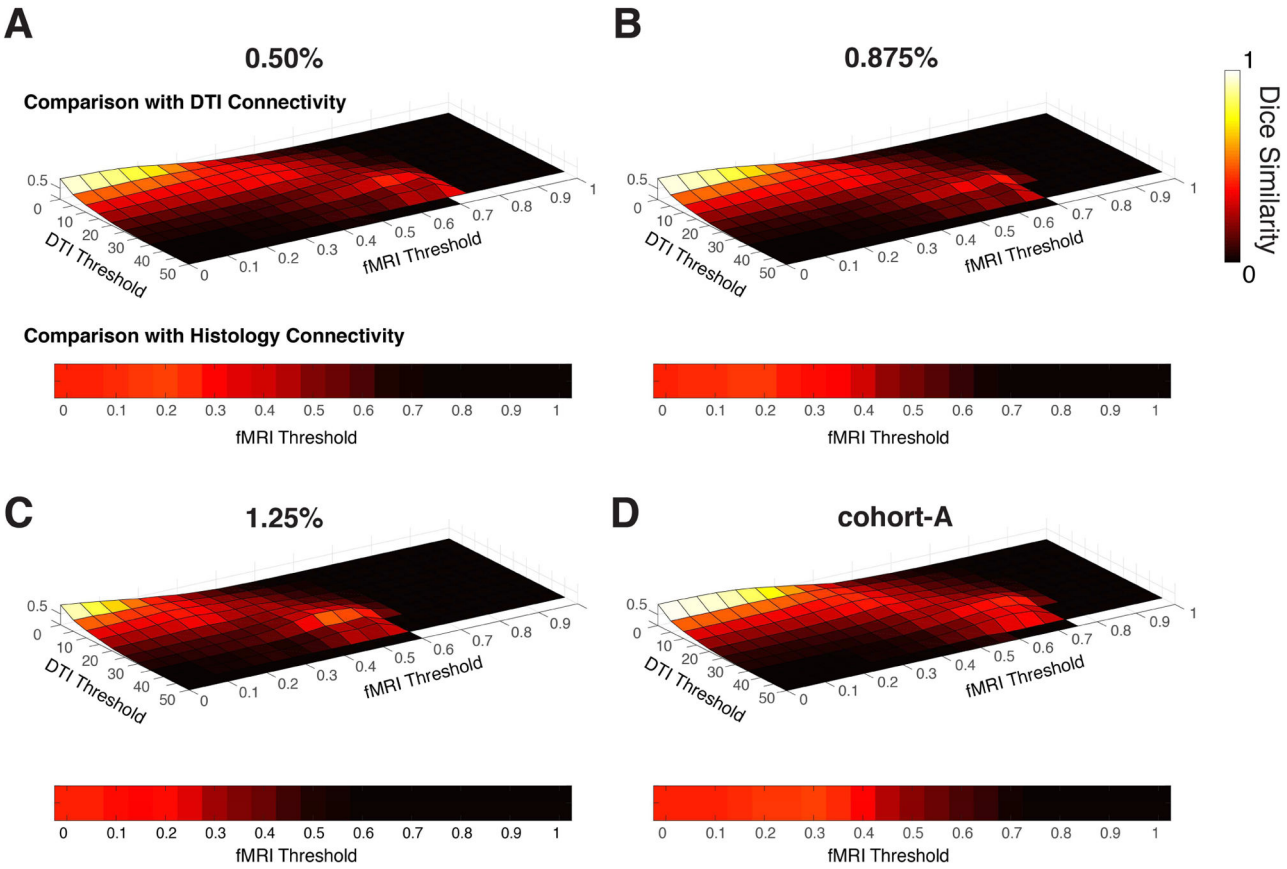

Figure 5:

Quantitative comparisons of rsfMRI with DTI and histological connectivity matrices. Sørensen-Dice measurements were computed for squirrel monkeys acquired at (A) 0.50%, (B) 0.875%, (C) 1.25% and for (D) cohort-A. (Top row of each subplot) DTI-to-rsfMRI Dice coefficients for varying DTI and fMRI thresholds. (Bottom of each subplot) Histology-to-rsfMRI Dice coefficients for varying fMRI thresholds.

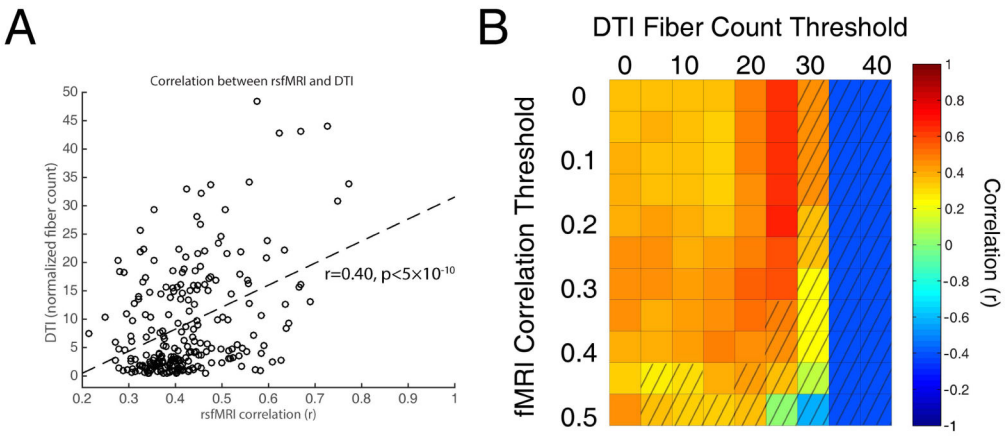

Figure 6:

Pearson's correlation between fMRI and DTI connectivity elements. (A) Scatter plot of GM-WM pairs with significant correlation values in Figure 2D; r=0.40 ($p<5\times10^{-10}$). (B) Distribution of correlation values between fMRI and DTI connectivity with varying fMRI and thresholds. Unshaded voxels indicate significant correlations with $p<0.05$. Average of significant correlations at various thresholds was computed to be 0.44.

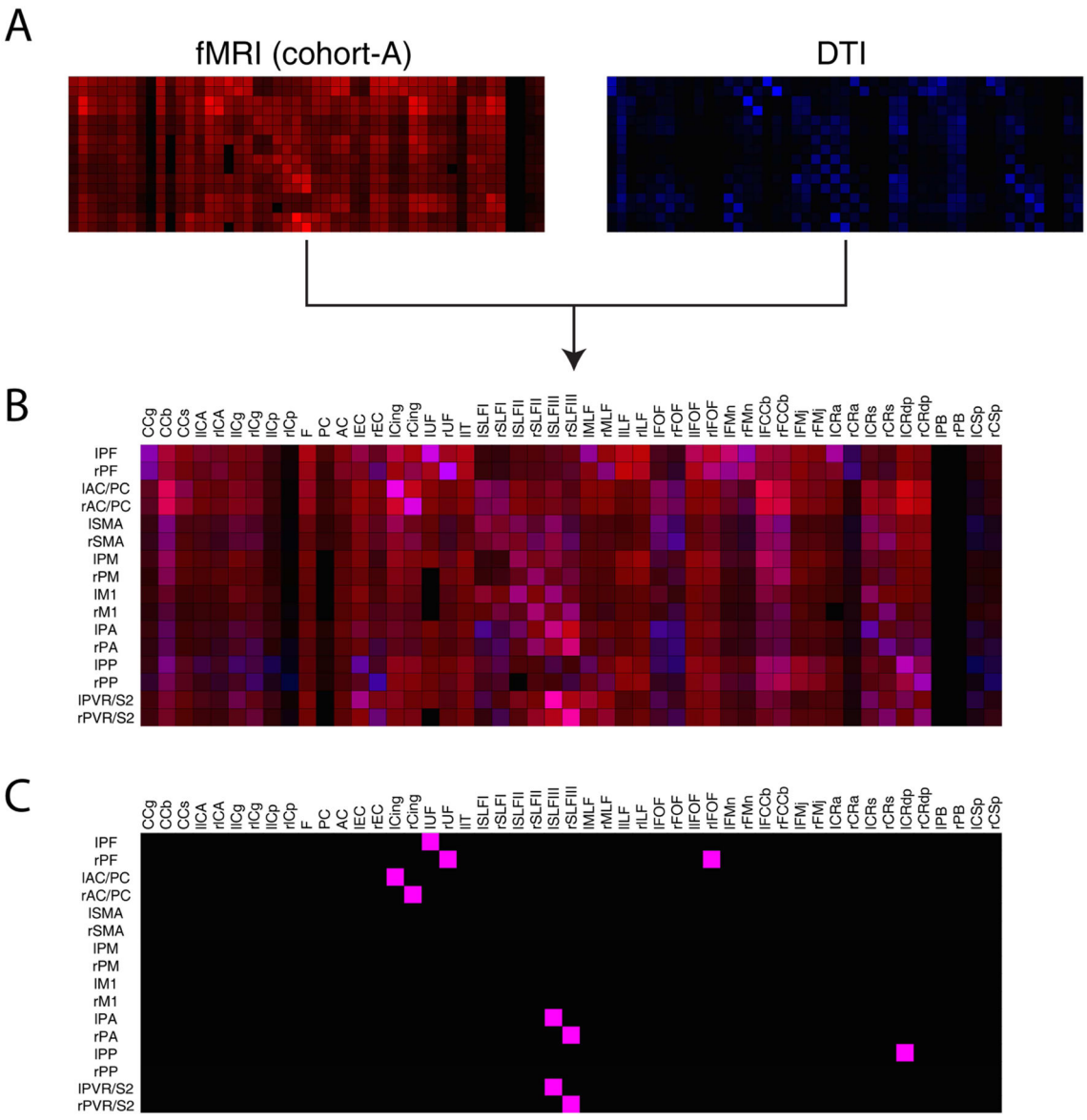

Figure 7:

Similarity comparison of rsfMRI with DTI connectivity of each individual GM-WM pair through RGB color overlay. (A) Normalized rsfMRI correlation (left) and DTI fiber count (right) matrices from Figure 2A-B are displayed as hues of red and blue respectively on a RGB scale. (B) Overlay of the red and blue connectivity matrices through additive color mixing. Maximal possible overlay would appear as the color of pure magenta with RGB elements of [1 0 1]. (C) Thresholded WM-GM pairs that exhibit highest degrees of similarity between the two modalities. Each WM-GM pair's red and blue pigments were thresholded by their respective 95th percentile value; connectivity pair elements in (B) with both red and blue pigments greater than their respective thresholds are displayed as magenta voxels, and as black voxels otherwise.

Table#1:

Quantitative comparison between fMRI connectivity map and DTI and histological connectivity maps with Sørensen-Dice metric

	DTI Connectivity				Histological Connectivity		
	Local Max Dice	**DTI Threshold ($thres_{dti}$>20)**	**fMRI Threshold ($thres_r$>0.05)**	**Random Permutation Probability**	**Local Max Dice**	**fMRI Threshold ($thres_r$>0.05)**	**Random Permutation Probability**
0.50% iso	0.42	30	0.60	0.0025	0.46	0.20	0.0000
0.875% iso	0.40	30	0.65	0.0073	0.45	0.15	0.0002
1.25% iso	0.50	30	0.45	0.0045	0.37	0.20	0.2806
Cohort-A	0.42	30	0.65	0.0034	0.46	0.30	0.0000